PAPER • OPEN ACCESS

Physics basis for the divertor tokamak test facility

To cite this article: F. Crisanti *et al* 2024 *Nucl. Fusion* **64** 106040

View the article online for updates and enhancements.

Physics basis for the divertor tokamak test facility

F. Crisanti[1,2,*], R. Ambrosino[1,3], M.V. Falessi[20], L. Gabellieri[1,4], G. Giruzzi[5], G. Granucci[1,6], P. Innocente[7,8], P. Mantica[6], G. Ramogida[1,2,4], G. Vlad[4], R. Albanese[1,3], E. Alessi[6], C. Angioni[9], P. Agostinetti[7,8], L. Aucone[10], F. Auriemma[7,8], B. Baiocchi[6], L. Balbinot[2], A. Balestri[11], T. Barberis[12], M. Baruzzo[4], T. Bolzonella[7,8], N. Bonanomi[6], D. Bonfiglio[7,8], S. Brezinsek[13], G. Calabrò[2], F. Cani[7,8], I. Casiraghi[6], A. Castaldo[4], C. Castaldo[4], M. Cavedon[10], S. Ceccuzzi[1,4], F. Cichocki[6], M. Ciotti[4], C. Day[14], C. De Piccoli[7,15], G. Dose[4], E. Emanueli[12], L. Frassinetti[16], L. Figini[6], V. Fusco[4], E. Giovannozzi[4], M. Gobbin[7,8], F. Koechi[17], A. Kryzhanovskyy[7], Y. Li[3,18], R. Lombroni[2], T. Luda[9], A. Mariani[6], P. Martin[1,7,19,22], C. Meineri[9], A. Murari[1,7], P. Muscente[7,15], F. Napoli[4], E. Nardon[5], R. Neu[9], M. Nocente[12], M. Notazio[2], S. Nowak[6], L. Pigatto[7], C. Piron[4], F. Porcelli[12], S. Roccella[4], G. Rubino[1,4], M. Scarpari[2], C. Sozzi[7], G. Spizzo[7,8], F. Subba[12], F. Taccogna[7,8], C. Tantos[14], D. Terranova[7,8], E. Tsitrone[5], A. Uccello[6], D. Van Eester[13], N. Vianello[7,8], P. Vincenzi[7,8], M. Wischmeier[9] and F. Zonca[20,21]

[1] DTT S.C.a.r.l., Frascati, Italy
[2] Department of Economics, Engineering, Society and Business Organization (DEIm), University of Tuscia, Largo dell'Università snc 01100 Viterbo, Italy
[3] Consorzio CREATE and the Dipartimento di Ingegneria Elettrica e delle Tecnologie dell'Informazione (DIETI) Università degli Studi di Napoli Federico II, Napoli, Italy
[4] ENEA Fusion and Technologies for Nucl. Safety Dept, C.R. Frascati C.P.65-00044 Frascati, Rome, Italy
[5] CEA, IRFM F 13108 Saint-Paul-lez-Durance, France
[6] Istituto per la Scienza e la Tecnologia dei Plasmi, CNR, Milano, Italy
[7] Consorzio RFX, Corso Stati Uniti 4 35127 Padova, Italy
[8] Istituto per la Scienza e la Tecnologia dei Plasmi, CNR, Padova, Italy
[9] Max Planck Institute for Plasma Physics, Boltzmannstr. 2 85748 Garching, Germany
[10] Università degli Studi di Milano-Bicocca, Milano, Italy
[11] École Polytechnique Fédérale de Lausanne (EPFL), Swiss Plasma Center (SPC) 1015 Lausanne, Switzerland
[12] Politecnico di Torino, Torino, Italy
[13] Forschungszentrum Jülich GmbH, Institut für Energie- und Klimaforschung—Plasmaphysik, Partner of the Trilateral Euregio Cluster (TEC) 52425 Jülich, Germany
[14] Karlsruhe Institute of Technology, Hermann-von-Helmholtz-Platz 1 76344 Eggenstein-Leopoldshafen, Germany
[15] CRF—University of Padova, Padova, Italy
[16] Fusion Plasma Physics, ECSS, KTH Royal Institute of Technology, Stockholm, Sweden
[17] UKAEA, CCFE, Culham Science Centre, Abingdon, Oxon, United Kingdom of Great Britain and Northern Ireland
[18] Swip, Southwestern Institute of Physics, PO Box 432, Chengdu, Sichuan 610041, China
[19] Department of Physics and Astronomy, University of Padova, Padova, Italy
[20] Center for Nonlinear Plasma Science and C.R. ENEA Frascati, C.P. 65 00044 Frascati, Italy
[21] IFTS, School of Physics, Zhejiang University, Hangzhou, China
[22] Centro Linceo Interdisciplinare 'B. Segre' dell'Accademia Nazionale dei Lincei, Rome, Italy

[*] Author to whom any correspondence should be addressed.

CrossMark

Abstract

This paper is dealing with the physics basis used for the design of the Divertor Tokamak Test facility (DTT), under construction in Frascati (DTT 2019 DTT interim design report (2019)) Italy, and with the description of the main target plasma scenarios of the device. The main goal of the facility will be the study of the power exhaust, intended as a fully integrated core-edge problem, and eventually to propose an optimized divertor for the European DEMO plant. The approach used to design the facility is described and their main features are reported, by using simulations performed by state-of-the-art codes both for the bulk and edge studies. A detailed analysis of MHD, including also the possibility to study disruption events and Energetic Particles physics is also reported. Eventually, a description of the ongoing work to build-up a Research Plan written and shared by the full EUROfusion community is presented.

Keywords: plasma, experiment, theory

(Some figures may appear in colour only in the online journal)

1. Introduction

Divertor Tokamak Test (DTT) is a tokamak with the complete magnetic system realized by superconductors coils, with a maximum vacuum toroidal magnetic field of $B_T = 5.85$ T at the plasma geometrical center, carrying plasma current up to $I_P = 5.5$ MA and with an overall magnetic driven pulse length up to 100 s [1]. The DTT poloidal system is composed by six central solenoid (CS) modules, by six external poloidal coils (PCs) and by five internal coils, all of them independently fed. The toroidal coils, the CS coils an two of the PC coils are realized using Niobium Tin (Nb_3Sn) and the rest of the PF are made by more standard Niobium Titanium (Nb_3Ti). This high flexibility in the poloidal circuits mirrors in the capability to obtain practically every kind of desired magnetic equilibrium configurations. Single Null (SN), X-divertor (XD) and Negative Triangularity (NT) (in order of priority) are presently under study by using the most updated modeling codes, like JINTRAC [2] or ASTRA [3, 4], and by using as transport models TGLF [5] or QuaLiKiz [6]. Double Null (DN) configurations are also in principle feasible, but a top divertor is not presently foreseen. It could be installed in a later phase, since there is space to allocate it on the Vacuum Vessel (VV) top [7, 8] The reference SN D-shaped toroidal cross section has a major radius $R = 2.19$ m, minor radius $a = 0.70$ m, an elongation $k \sim 1.7$ and an average triangularity at the separatrix $\delta^{SEP} \sim 0.48$. In order to fulfill its main target, i.e. studying the integrated core-edge power exhaust problem, DTT is equipped with an auxiliary heating power, coupled to the plasma, up to a nominal level of 45 MW that is provided by a mix of three different heating systems: Electron Cyclotron (ECRH), up to 29 MW at 170 GHz, Ion Cyclotron (ICRH), up to 6 MW in the range 60–90 MHz and Negative Neutral Beams (NNBI), up to 10 MW at 510 keV [8] (installed powers). This heating power allows to get $P_{SEP}/R \sim 15$ MW m^{-1} (where P_{SEP} is the power crossing the separatrix) matching with the ones expected on ITER and the maximum value that will be allowed by the present materials on DEMO. The simultaneous use of ICRH and NNBI allows generating an Energetic Particles (EPs) population with energy density comparable with that of the core plasma and characteristic energy more than the critical energy; that is the energy at which the EP slowing down rate on thermal electrons balances the pitch angle scattering rate of thermal ions [9]. These are the distinctive features of reactor relevant burning plasma [10, 11] that will be accessible in DTT.

The primary mission of DTT is to study the plasma exhaust and the tokamak divertor performance with a divertor power and particle flow conditions relevant to ITER [12] and DEMO [13, 14], and to perform these studies in regimes in which high performance plasma core and large Scrape Off Layer energy (SOL) flux will have to coexist. To attain this objective, all the Plasma Facing Components (PFCs) will be made of actively cooled tungsten: the divertor will be realized by shaped W monoblocs (to maximize the surface and to protect the monoblocs corner), whilst the First Wall (FW) will be realized either by monoblocs (in regions where high energy fluxes are foreseen) or by W coatings. The VV is a double shell chamber with water flowing inside. During the experiments the cooling water for the FW and the VV will be at a temperature of 80 °C. In four toroidal location it is foreseen the possibility to facilitate the use of Test Module Divertor (TMD) to quickly test new ideas for the divertor materials and partially for the Plasma Facing Units (PFUs) shaping. An extensive use of fluids codes (like SOLEDGE and SOLPS) has allowed to design a first DTT divertor capable to fit with all the three planned main configuration (SN, XD, NT) and to study at best their most important features. The possibility to achieve detached plasmas has been observed. Although DTT, working at high performances, is foreseen to have a medium value of β_N, by working at reduced performances ($B_T = 3$T to best use the second harmonic of the ECRH) high β_N advanced confinement scenarios will be accessible. In this way, in addition to

its primary mission, DTT will be complementary to JT-60SA to study advanced confinement scenarios in a full W environment. Working in parallel at ITER [15] and with similar PFU and main heating, DTT will also support the ITER experiments and/or tackle problems such as, for instance, the disruption mitigation. To this end, the VV and the other mechanical components have been designed to sustain a very large number of disruptions. DTT has been designed to provide a facility for high performance tokamak physics and to address core confinement and stability issues in a variety of plasma configurations, all along the ITER life and during future fusion reactor design. Consequently, to fulfill this task, DT will need the support and the ideas of the largest possible scientific community. For this reason, a first version of the DTT research plan is presently under realization with the contribution of about 100 European scientists, with the idea of including a larger international community in the development of the following versions.

2. DTT Reference plasma scenarios

In order to reproduce, on a scaled experiment, the most important core and edge dimensionless physics parameters, the normalized pressure β, the normalized Larmor radius ρ^* and plasma collisionality ν^*, plus the average temperature should be preserved [16, 17].
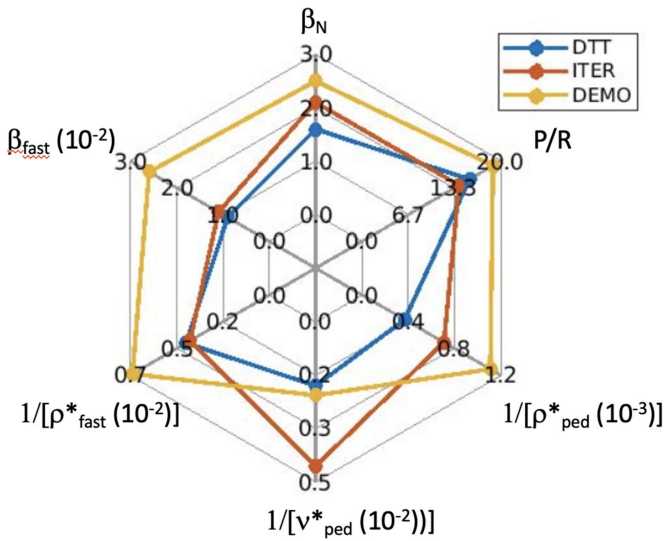
However, using the collection of ρ^*, β, ν^* and T, on the other hand, makes it impossible to define a non-trivial set of similarity experiments. Thus, the attempt of extending the conventional similarity argument to burning plasma relevant experiments yields the apparent paradox that only the trivial solution exists, for which ITER, for instance, relevant burning plasma physics issues can be addressed in ITER only. By considering these facts, the reference DTT plasma scenarios have been designed by using the 'weak similarity' approach [18, 19], which has allowed to suitably rescale plasma parameters with respect to those of ITER, while still addressing the relevant integrated physics. 'Weak' here is to be intended as in its rigorous mathematical definition, i.e, an argument reproducing a general result under less stringent assumptions, which are relaxed in a controlled way and yield the original 'strong' result in the appropriate limit. This can be done in two ways: one is based on assuming that ρ^*, R^ε, β and ν^* are fixed (to those in ITER) and appropriately rescaling T with respect to the ITER reference value; the other assumes that that $\rho^* R^\varepsilon$, β and τ_{SD}/τ_E (being τ_{SD} and τ_E respectively the EPs particle slowing time and the energy confinement time) are fixed (to those in ITER) and, as in the former case, appropriately rescales T with respect to the ITER reference value. One easily obtains that the two approaches give very similar results; however, while the first approach is aimed at preserving core-edge nonlinear plasma couplings, the second one is justified in terms of focus on the physics of plasmas with predominant fusion alpha particle self-heating. Since the main target of DTT is the study of the integrated core-edge physics to find a solution for the power exhaust problem, the former approach has been initially used to work out the main machine parameters.

The extensive use of state-of-the-art integrated modeling tools, such as JINTRAC or ASTRA, with the transport models TGLF or QuaLiKiz has confirmed the robustness of the initial parameter selection. In table 1 and in the spider plot (figure 1) some of the most important DTT parameters (the normalized ρ^* and ν^* evaluated at mid radius and at the pedestal, the normalized total β_N, the central EPs normalized Larmor radius and β, the total power and the total power normalized to the plasma machine major radius, the density Greenwald density limit, the operational q_{95}) are reported versus the ones expected for ITER and DEMO. One can see that the DTT parameters are of high relevance for both ITER and DEMO. In particular, the combination of high current (i.e. high confinement) and high power (i.e. high temperatures) allows the DTT plasmas to combine high density with low collisionality at the pedestal top and high collisionality at the separatrix, matching the conditions expected in a tokamak reactor. In combination with the full tungsten walls and with reactor relevant EP dimensionless parameters, these properties put DTT in a unique position to address critical open questions on the integration among core, edge (pedestal) and SOL, still a big challenge towards the definition of the operational point of a fusion reactor. Furthermore, DTT will be capable of addressing many of the EP physics issues that are peculiar to reactor relevant fusion plasmas; e.g. the unique role of EP as mediators of spatiotemporal cross-scale couplings in fusion plasma self-organization [10, 11]. Integrated modeling using JINTRAC and ASTRA has allowed to work out the detailed expected profiles and their temporal evolution for temperatures T_e and T_i, density n_e, current density J, rotation ω_{tor} and two impurities (a light one i.e. Ar, Ne or N, and a heavy one, i.e. W). Details of the methodology of these simulations can be found in [20, 21]. The transport equations were solved within $\rho_{tor} = 0.94$ (pedestal top) and the pedestal calculated with EUROped [22]. TGLF-SAT2 was used as turbulent transport model and FACIT [23] for impurity neoclassical transport. With respect to the simulations in [20], the simulations presented here have an updated equilibrium, following the recent decision to move upwards the plasma by about 12 cm to accommodate a new divertor design, and a broader ECH deposition, optimized for the use of pellet fuelling, as discussed in [24]. Plasma edge boundary conditions were tuned to obtain SOL parameters that guaranteed divertor plasma detachment; the light impurity concentration required to obtain these conditions at the divertor implies a radiated power fraction in the confined region of about 30%. Full power scenarios have been simulated, as well as those scenarios with reduced power, magnetic field and current, that will characterize the early phases of operations.

For the full power, full field, full current scenario, at flat-top, values of $T_{e0} \sim 12$ keV, $T_{i0} \sim 10$ keV, and $n_{e0} \sim 2.5 \ 10^{20}$ m^{-3} are reached in the core. Figure 2 shows the predicted profiles of the main plasma parameters for the full power scenario (E1) using both the TGLF SAT2 and the QuaLiKiz models. Figure 3 shows the power deposition profiles. It has to be noted that T_e is slightly larger than T_i, which is a consequence of the dominant electron heating and of high ion stiffness. It is also worthwhile mentioning that the DTT NNBI will be super-Alfvénic, mimicking conditions of ITER

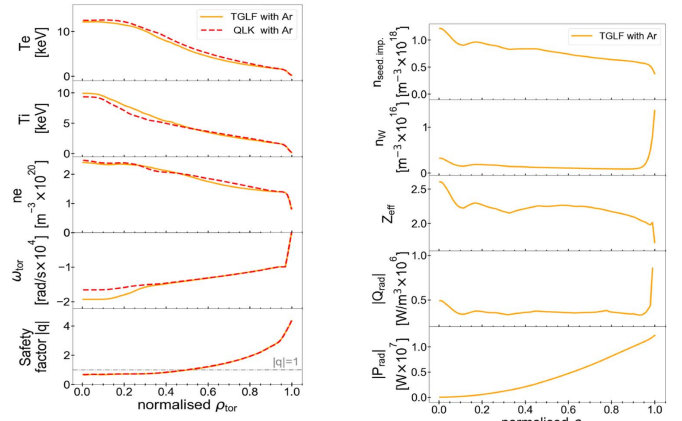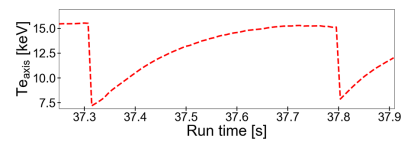**Table 1.** DTT, ITER and DEMO main parameters comparison.

	DTT	ITER	DEMO 2018
P_{sep}/R (MW m^{-1})	15	14	18.9
P_{tot} (MW)	45	150	450
β_N (%)	1.8	2.1	2.5
ρ^* at mid-radius (10^{-3})	4.1	2.0	1.5
ν^* at mid-radius (10^{-2})	0.75	0.3	0.3
ρ^* at pedestal (10^{-3})	2.3	1.4	0.8
ν^* at pedestal (10^{-2})	7	2.2	8
q_{95}	3.1	3.2	3.89
n_{GW} (10^{20} m^{-3})	3.6	1.2	0.66

Figure 2. Radial profiles for the E1 scenario flat-top phase: (*a*) of the electron and ion temperatures, electron density, toroidal rotation, and safety factor absolute value, with turbulent transport calculated by TGLF SAT2 (solid orange lines) or by QLK (dashed red lines) with argon; (*b*) profiles of the seeding impurity and tungsten densities, effective charge, radiative power density, and radiative power, calculated by TGLF and FACIT.

Figure 1. Spider plot of some important parameters for DTT, ITER and DEMO.
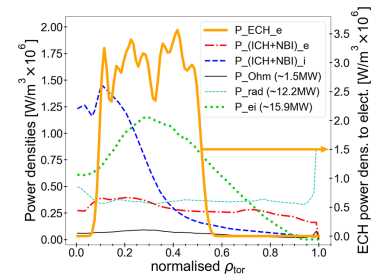
Figure 3. Radial profiles of power densities for the full power SN scenario: ECRH power deposited to electrons P_{ECRHe}, NBI and ICRH power deposited to electrons $P_{(ICRH+NBI)e}$, NBI and ICRH power deposited to ions $P_{(ICRH+NBI)i}$, Ohmic power P_{Ohm}, radiative power P_{rad}, and thermal exchange power between electrons and ions P_{ei} (from the TGLF-SAT2 simulation).

Table 2. Parameters of the scenarios simulated in figure 8.

	Sc. A	Sc. C	Sc. E
I_{pl} [MA]	2.0	4.0	5.5
B_{tor} (T)	3.0	6.0	6.0
$<n_e>$ sep (m^{-3})	3.5	4.5	8.0
P_{aux} (MW)	8	20	50
$<Z_{eff}>$ ped top	1.4	2.1	2.7
Impurity	N	Ne	Ne

Figure 4. Time evolution of the electron temperature at the plasma center T_{e0} during a sawtooth.

tangential beams. W is strongly screened and does not accumulate in the center. In the configurations at high current and high performances the q profile features a large central zone where $q \sim 1$, consequently large sawteeth with a frequency $\sim$1.5–2 Hz characterize the inner half of these high current plasmas (see figure 4). In the full power standard H mode scenario DTT has a very high-pressure pedestal. Utilizing existing type-I ELM scaling laws, we expect $\Delta W_{ELM}/W_{ped} \approx 9.6\%$ and hence $\Delta W_{ELM} = 0.34$ MJ [20].

The edge is very opaque, which makes very difficult to feed the plasma density by the standard gas injection. For this reason, fueling the full power scenarios requires pellet injection: obliquely injected pellets from the High Field side, with dimensions and velocities $r = 1$ mm, $v = 516$ m s^{-1} and

frequencies of 10–20 Hz, are found suitable for maintaining the required density profile [24]. Simulations of the full-time history of the discharge are in progress using ASTRA/TGLF and METIS, to design best paths to access the H-mode, and to optimize the q profile during the current rise [21]. Finally, DTT configurations with NT (average $<\delta^{SEP}> \sim -0.135$) have been studied both with first-principle simulations [25] and by specific experiments on TCV and AUG using the same shapes foreseen for DTT [26, 27]. Simulations either using the gyrokinetic code GENE or the quasi-linear model TGLF do not show any effect of the change of δ on transport inside $\rho_{tor} \sim 85$. However, both in TCV and AUG positive effects
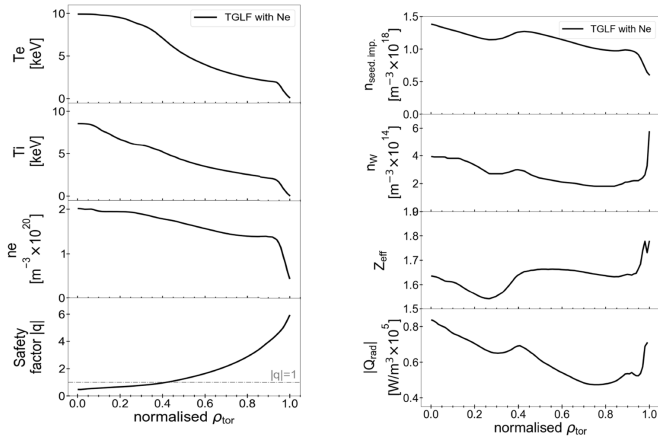
Figure 5. Radial profiles for the C SN scenario flat-top phase (*a*) of the electron and ion temperatures, electron density and safety factor absolute value and (*b*) of the seeding impurity (Neon) and tungsten densities, effective charge and radiative power density, with turbulent transport calculated by TGLF and neoclassical by FACIT.

Figure 6. The three main DTT configurations.

are seen in the edge region, in L-mode being localized outside $\rho_{tor} = 0.9$ and in the SOL. These edge effects allow the recovery of central parameters typical of an H-mode. They could be present also in DTT but are difficult to predict by present core models (see discussions in [28]). Finally, profiles for an earlier phase scenario with full vacuum toroidal magnetic field ($B_{tor} = 5.85$ T), but with reduced plasma current ($|I_{pl}| = 4.0$ MA) and with an installed external power of 20 MW (with 16 MW by ECRH and 4 MW by ICRH) are shown in figure 5. This power is very marginal to enter H-mode, depending on the amount of radiated power. In the following we keep radiation low enough to get above L-H threshold, but an alternative simulation would be possible with more radiation and L-mode. The modeling was performed using TGLF-SAT2 as turbulent transport model and FACIT for impurity neoclassical transport, within an ASTRA simulation. The transport equations were solved within $\rho_{tor} = 0.89$. Neon was used as seeding impurity. The pedestal pressure was calculated by the Europed model. The radial profiles of T_e, T_i, n_e, safety factor absolute value $|q|$, seeding impurity density $n_{seed.imp}$ tungsten density n_W, effective charge Z_{eff}, radiative power density Q_{rad} are shown in figure 5. Toroidal rotation was set to 0 due to the lack of NBI.

3. Power exhaust strategy and reference divertor

Power exhaust modeling was performed using linear fluids edge codes coupled with kinetic codes for neutrals. SOLEDGE2D-EIRENE [29, 30] and SOLPS-ITER have been carried out to define the divertor shape capable of allocating the standard SN divertor configuration, the alternative XD, their long leg variants and also NT equilibria, see figure 6 where a representative figure is shown for all three main configurations. It has to be noticed that for any of the configurations shown in figure 6, several different features can be varied: the elongation, the plasma position the low and the bottom triangularity, and especially the leg length and the proximity
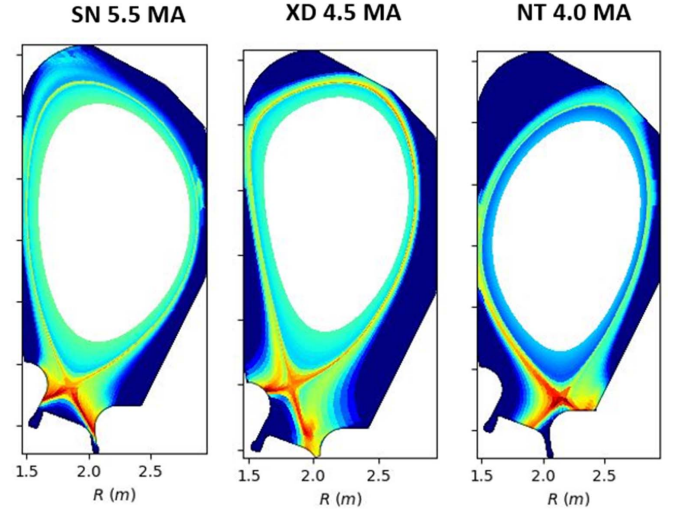
of the second field null for the XD configuration. This large flexibility in controlling the plasma shape is due to the fact that the PCs are independently fed and that on the bottom of the machine 3–4 (the exact number has not yet been decided) coils are allocated to optimize the local divertor magnetic topology.

Edge modeling has been done using transport parameters in agreement with present scaling laws [31, 32] and with the radial profiles tuned to reproduce present JET and C-mod experiments [33]. This provides, as much as possible, a reliable and robust estimation of temperatures and densities up to the top of the pedestal, in conditions approaching those of DTT. A comparison between different divertor shapes in terms of power exhaust performances have driven to the present design of the first DTT divertor [34]. The selected shape has a flat dome and two narrow necks where the strike points of the SN configuration can be allocated. This choice is compatible with all the reference equilibria of figure 6 and will allow experiments with a full open divertor (for instance in the NT configuration) and of experiments with the leg positioned within a narrow neck as well.

The selected divertor shape will allow operation at full power with noble gas impurity seeding by neon or argon in Partially Detached (P/D) conditions, with a reasonable level of impurity content inside the separatrix ($n_{Ar}/n_e = 1\%$ or $n_{Ne}/n_e = 3\%$–4%) down to $n_{e,sep} = 8 \cdot 10^{19}$ m^{-3} allowing plasma scenarios with a Greenwald density fractions $n/n_G = 0.5$ [35]. The predicted temperature at the separatrix is higher ($T_{sep} \approx 200$ eV) than in the present experiments. Modeling has also shown that the most critical condition is getting a low plasma temperature in front of the target in order to control tungsten influx, while the maximum power load is easily below the limit (20 MW m^{-2}) allowed by the tungsten monoblocks of the divertor. Better performance in terms of lower impurity content seems possible by operating the divertor in Full Detached (F/D) conditions but this reduces the neutral pressure at the pumps entrance. This point is illustrated in figure 7, where two P/D and F/D SN full power cases
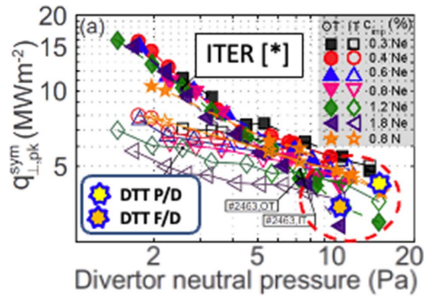
Figure 7. DTT detached condition compared with the ITER ones. Circle indicates detached situation.

Figure 8. Z_{eff} profile for three different configuration P/D and F/D.

are reported in comparison with ITER conditions [36]. As in ITER, detachment is achieved with a very high neutral pressure (10–20 Pa), but this pressure is nearly halved moving from P/D to F/D. Interestingly, the better performances in F/D is achieved by a higher level of radiation, which does not correspond to a higher impurity content but to a wider low temperature region in the divertor and a high radiation close to the X-point, realizing conditions similar to those of the X-point radiator (XPR) configuration. The detailed neutrals distribution has been used to realize a complete simulation of the pumping condition [37] for the characterization of cryopumps system and the optimization of the sub-divertor region, in order to maximize the pumping capability. The achievement of P/D and F/D conditions is easier at similar $n/n_G = 0.5$ in the initial phase of the DTT operation, not only because of the reduced available power, but also due to the higher transport expected at lower toroidal magnetic field and plasma current. Indeed, some modifications are foreseen in terms of operating scenario; in particular, in the initial phase with $B_t = 3$ T, nitrogen gas seeding provides good performance with low contamination and the pumping speed must be reduced to avoid a top pedestal density too high. Figure 8 shows the Z_{eff} required to obtain partial and full detachment in three different operational phase scenarios: (a) low current and low field; (b) low current and reference field; (c) high current and high field. The results have been obtained by a simulation performed by the SOLEDGE2D-EIRENE code and by using Neon as a controlled impurity. As it can be observed, the Z_{eff} value increases when the plasma performances increase and it tends to peak when approaching the separatrix. The scenario details and the modeling activity are fully described in [20], and the main scenario parameters are listed in table 2.

4. MHD Stability

Simulations for MHD stability studies are carried out for DTT Full Power [38] (on axis magnetic field $B_0 = 5.85$ T and plasma current $I_p = 5.5$ MA) and reduced current/field ($B_0 = 2.9$ T, $I_p = 2.0$ MA, also named Day0) operational scenarios, utilizing the positive triangularity (PT) configuration (figure 9 shows the safety factor and pressure profiles for the two scenarios, red continuous curves for Full Power, blue dashed curves for Day0). To this aim, plasma equilibria, as obtained by 1-D transport solvers (e.g. JINTRAC or ASTRA)
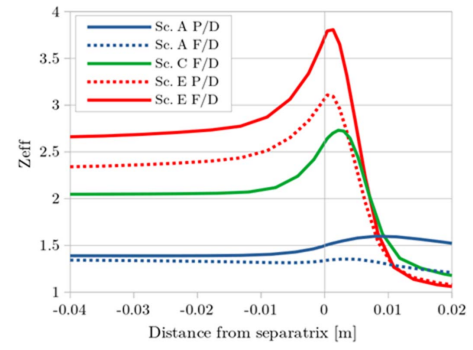
have been refined obtaining high-resolution fixed boundary equilibria using the equilibrium solver CHEASE [39]. This code supplies the equilibrium quantities and the metric tensor to different stability codes; for the purpose of these analyses, the MARS [40] code has been used. MARS solves the full linear, resistive MHD equations, in a two-dimensional, axisymmetric toroidal geometry defined in flux coordinates (s, χ, φ). Here $s = (1 - \psi/\psi_{axis})^{1/2}$ represents the poloidal radial-like normalized coordinate, such that $s = 0$ on axis and $s = 1$ on the plasma edge; the variable ψ is the poloidal flux function, χ is a generalized poloidal angle assigned by choosing the Jacobian of the transformation from Cartesian to flux coordinate and φ is the geometrical toroidal angle. MARS can also consider a vacuum region between the plasma last closed surface and a perfectly conducting wall, assumed to be conformal to the plasma last closed magnetic surface. The outcomes of thorough electromagnetic and transport investigations [20], reveal crucial parameters related to MHD in the scenario. In particular, considering the Full Power scenario, the safety factor q exhibits a relatively flat profile around the plasma center, with its value on the axis (q_0) being approximately $q_0 \approx 0.7$. At the plasma edge, $q_{95\%} = 2.8$, and the $q = 1$ surface is located at a rather large radius (see figure 9). The toroidal β, defined as $2\mu_0 <p>/B_0$, is $\beta = 1.89\%$, where μ_0 is the vacuum permeability constant, B_0 the on axis magnetic field and $<p>$ the pressure averaged on the plasma volume. The pressure peaking $p_0/<p>$, with p_0 the pressure on axis, is approximately equal to 4. Because of the $q = 1$ surface inside the plasma, an internal kink is expected: indeed, this result is confirmed by the MARS code, as can be seen by the left-hand side (l.h.s.) of figure 10. For the example shown, a vacuum region around the plasma is considered, placing the ideally conducting wall at $r_{ext} = 3$ (here r_{ext} is defined as the ratio *b/a*, where *a* is the plasma minor radius and *b* is the wall minor radius). This value, for the purpose of such investigations, can be considered as a no-wall situation. The growth rate γ of the internal kink (normalized to the inverse of the Alfvén time $\tau_{A0} = R_0 \sqrt{(\mu_0 \rho_0)}/B_0$, with ρ_0 the on-axis mass density), is shown in the r.h.s. of figure 10 as a function of the wall position r_{ext}. It is worth noting that such a large $q = 1$ position poses some concern on the large sawtooth crashes that could be induced by such an internal kink mode. On the other hand, the addition of sawtooth model in a transport code is a work in progress which could result in a $q = 1$
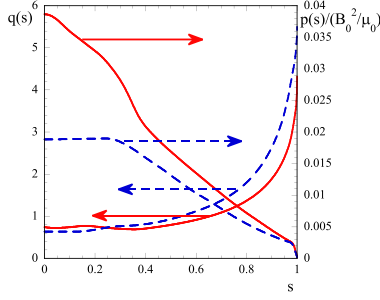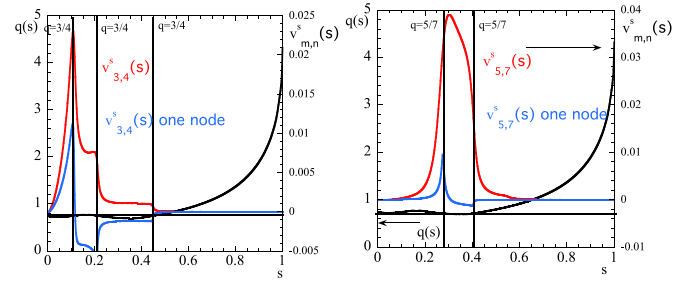
Figure 9. Safety factor and pressure profiles for the Full Power (red, continuous curves) and Day0 (blue, dashed curves) equilibria.
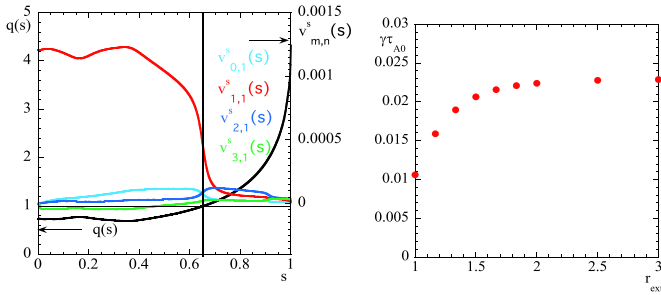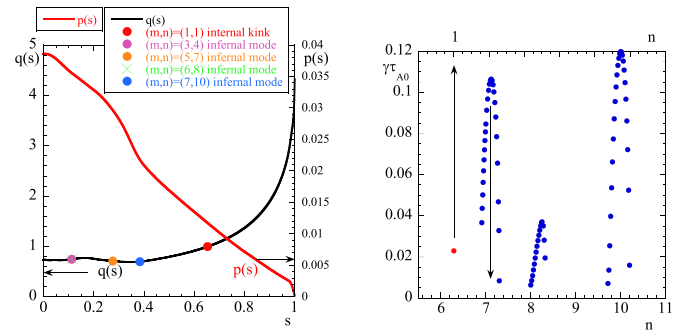

Figure 10. L.h.s: contravariant components of the perturbed velocity $v^s_{m,n}(s)$ for the internal kink $(m,n) = (1,1)$ and the safety factor q vs s at $r_{ext} = 3$. R.h.s: internal kink growth rate normalized to the inverse of Alfvèn time τ_{A0} ($\tau_{A0} = R_0\sqrt{(\mu_0\rho_0)}/B_0$), ρ_0 is mass density) vs the wall position.

Figure 11. L.h,s: contravariant component of the perturbed velocities $v^s_{m,n}(s)$ for the $(m,n) = (3,4)$ and $(m,n) = (5,7)$ infernal modes: main perturbation (red) and single radial node perturbation (blue).

Figure 12. L,h,s: position of the internal kink and infernal modes on the safety factor $q(s)$ and pressure profile $p(s)$. R.h.s: oscillatory behavior of the infernal modes growth rate, the red dot is the internal kink of the growth rate.

smaller radius, thus allowing a better control by external heating sources [20]. Further MHD stability investigations have continued increasing the toroidal mode number n where the so-called infernal modes have been evidenced. These modes are known to be responsible for limiting the achievable performance of tokamak devices [41]. The infernal mode is a pressure driven internal MHD instability, characterized by low to intermediate toroidal n and poloidal m mode numbers, which is excited in a region of low shear and high-pressure gradient. Examples of radial perturbed velocities $v^s_{m,n}(s)$ for infernal modes as obtained by MARS for this scenario are presented in figure 11. The position of the infernal modes w.r.t the safety factor profile is represented in figure 12 l.h.s. Moreover, the oscillatory behavior of the infernal modes growth rate, with respect to n (here considered as a continuous parameter), is depicted in figure 12 r.h.s.

For comparison, the growth rate of the internal kink is also reported with a red dot. As a conclusion, the infernal modes oscillatory behavior in n makes it difficult to predict which n value will give the most unstable mode. When resistivity is added in the analysis, the qualitative and quantitative behavior of the mode exhibits little changes, and no specific resistive modes are observed. The resistivity barely affects the growth rate of the resistive internal kink that slightly decreases when $1/S$ (the inverse of Lundquist number) decreases, (see figure 13). Similar analyses have been performed for the Day0 scenario, as for the Full Power scenario, the internal kink mode also exists in this scenario, because q_0 is below unity (see

figure 9). On the contrary, infernal modes disappear because the pressure gradient is almost negligible in the region where the magnetic shear is small. Sensitivity analysis on relevant quantities such as the safety factor on axis q_0 and β has been carried out as well for the Full Power scenario, to test stability robustness [38]: first q_0 and then β are varied while the other parameters are kept about constants (within 10% of the nominal values). The overall picture of the unstable modes does not change, and relevant external modes are obtained only when the physical quantities have values far from the nominal case. As an example, in figure 14 a more realistic case, where $q_0 \approx 1.2$ and $q_{95\%}$ is kept fixed, has been chosen and β_N has been varied (here β_N is the normalized β, defined as $\beta_N = \beta/I_p/(aB_0)$) [42]. Figure 14 (l.h.s.) depicts the growth rate as a function of β_N; it gives a flavor of what is the (β_N, γ) range of variability ($\beta_N \approx 3.05 \approx 2.4p_0$, $\beta_N \approx 3.73 \approx 3p_0$) defining instability for such ideal kink modes. Figure 14 (r.h.s) represents the growth rate for the $n = 1$ ideal kink mode vs r_{ext} (the conducting wall position), for different β_N. Study of the dynamics and stability of the Tearing Modes (TMs), a key issue to assess DTT plasma performances, has been done. These resistive helical unstable perturbations, driven by a local reduction of the bootstrap current and growing as magnetic islands, can degrade the confinement leading to disruptions for large island width. The TM dynamics has been calculated for different realistic guess values of the tearing stability parameter Δ'_0. Positive values simulate the TM onset
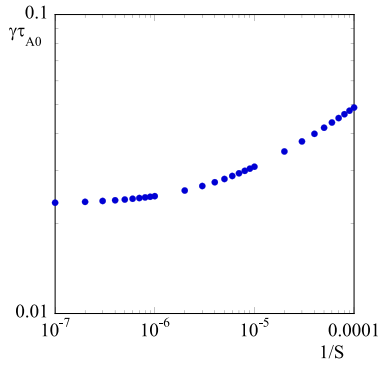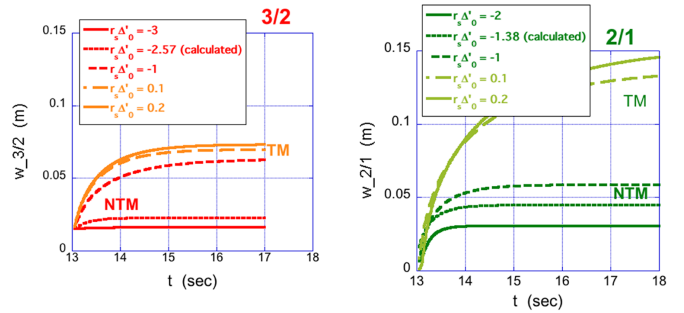
Figure 13. Resistive internal kink growth rate normalized to the inverse of the on axis Alfvèn time τ_{A0} versus the normalized resistivity (inverse of the Lundquist number S).
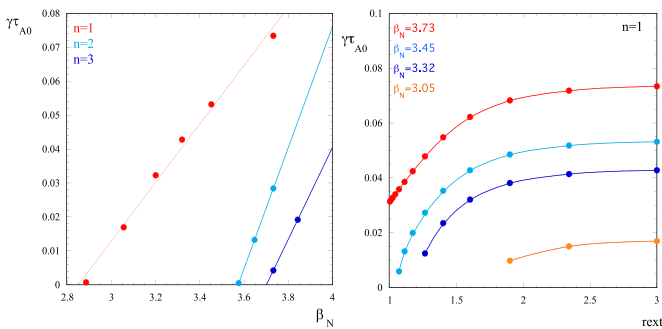
Figure 14. L,h,s: growth rate vs β_N for different toroidal mode number n for a more realistic case where $q_0 \approx 1.2$. R.h.s: growth rate vs r_{ext} for $n = 1$ and different β_N.

Figure 15. (N)TM sizes evolutions for 3/2 (left) and 2/1 (right) modes located at the resonant positions r_s considering different Δ'_0 values.

driven by the current density gradient, while negative values are associated to the Neoclassical Tearing (NTM) driven by seeded magnetic perturbations created for example by large sawtooth periods [43]. Evolutions and stabilization up to suppression of the main 3/2 and 2/1 modes, located at significantly off-axis positions in the full power scenarios at 5.4 MA and 5.8 T, are predicted using the NTM module [44] integrated in both the ETS (European Transport Simulator) [45] and the JETTO code [46]. In figure 15, time widths of 3/2 and 2/1 modes are shown for different Δ'_0 prescribed and calculated values. Predicted full island size ranges are found between 0.016 m and 0.075 m for 3/2 and between 0.03 m and 0.15 m for 2/1. NTM can be controlled/suppressed replacing the loss of bootstrap current by local current driven by ECCD in co-current with the plasma current direction. To achieve this goal in DTT, EC upper launchers are used to deliver up to 7.2 MW at 170 GHz with good current drive efficiency at the 3/2 and 2/1 surfaces. Unphased (CW injection) and phased (modulated injection) EC power can provide a good NTM control. Particularly, less EC power is needed with modulated injection with respect the CW case, for island size less than EC current density width. Both the 3/2 and 2/1 TM can be fully stabilized up to $w = 0$ in less than 1.4 s with EC CW power $\leqslant 1.5$ MW, applied when the island width is less than 0.03 m.

5. EPs

DTT will be equipped by three different heating systems, with predominant electron heating. However, the ICRH and NNBI will also heat ions and will generate an important population of EPs in an energy range relevant for ITER and DEMO. NNBI geometry and injection angles have been chosen to minimize prompt and magnetic ripple induced losses, while energy was fixed to satisfy optimal conditions for excitation of the Alfvénic fluctuation spectrum with proper frequency and wave number. In particular, these conditions require the use of a super-Alfvénic beam. The dynamics of EPs produced by the different heating systems is of crucial importance for various aspects of the DTT design. In particular, EP losses could damage PFCs and must be investigated carefully. This aspect has been explored both by ORBIT [47] and ASCOT [48] simulations. The Hamiltonian feature of ORBIT has been used to calculate losses due to the precession-bounce resonance of trapped energetic ions with the toroidal field ripple. By tailoring energy and injection angle of the NNBI system, these losses have been minimized; ORBIT has shown the presence of two 'hot spots', which correspond respectively to the injection and exit angle of the beam [49]. The ASCOT code allows the representation of realistic DTT NNBI sources, represented beamlet-by-beamlet including their 3D divergences. ASCOT is used to follow EPs in realistic geometry up to the machine FW, taking into account collisions in order to investigate beam EP confinement and losses [50]. Finally, the interaction of EPs with Alfvén Eigenmodes (AE) can lead to increased particle losses and, therefore, a careful kinetic analysis is required [51]. The general theoretical framework for the self-consistent analysis of all the aforementioned physics [11] involves self-consistent non-linear gyrokinetic simulations and the use of a realistic AE spectrum as input to test particle transport codes, in order to calculate the impact of wave-particle interaction on the EP losses [6, 52]. ASCOT simulations [31] showed a very good absorption of NNBI in the full power, reference target plasma (E1). EP losses are negligible with an axial-symmetric magnetic field, with the majority of power being absorbed by plasma electrons ($\sim 60\%$). NNBI is capable of providing limited torque and to drive current in the order of 25 kA MW^{-1}.
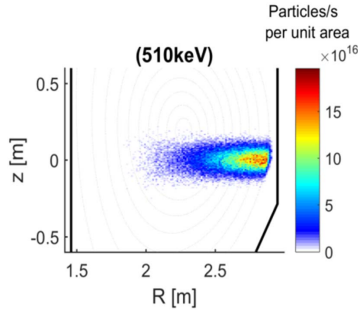
Figure 16. Poloidal projection of NBI ionization flux for DTT full power plasma (E1) with ASCOT.
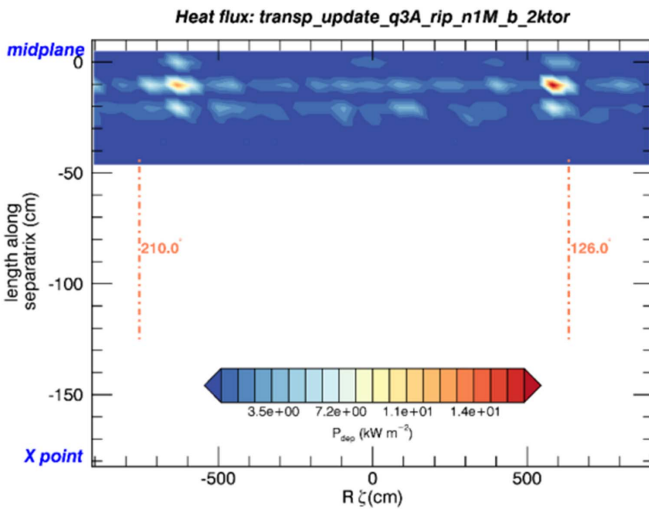

Figure 17. Map of the power load on the separatrix, calculated with a 1 million particle. Full power, single null DTT scenario. The two dashed lines correspond to the injection and exit toroidal angles of the NBI: hot spots form near these angles.

At lower density, shine-through will pose limitations for NNBI operation. Figure 16 shows the ionization flux, calculated by the BBNBI module [53] of the ASCOT suite of codes, for the full power (E1) plasma scenario. The initial orbits of the newly born fast ions have been investigated in [54] through the analysis of the Constant of Motion (CoM) phase space.

DTT NNBI EPs are mainly characterized by passing orbits, with a small fraction of trapped orbits, while non-standard orbits are excluded for DTT reference plasma E1. Prompt losses resulted negligible, in accordance to ASCOT full orbit-following simulations and with previous ORBIT estimates. This is due to the optimization of the NBI geometry to minimize both prompt losses (which are mainly passing particles with poloidal injection angle $\theta \neq 0$) and the fraction of trapped particles, which interact with the TF ripple via the mechanism of precession-bounce resonance. Recent ORBIT simulations with 10^6 test particles allowed to assess the EP losses via the resonant mechanism [55], which are relatively low, 0.065% of the initial NNBI population in the full power plasma (E1) scenario. Nevertheless, despite the overall low losses, energetic ions produce two very localized patterns, a.k.a. 'hot spots', corresponding approximately to the beam injection

and exit toroidal angles. The first hot spot is mainly due to prompt losses/passing particles, while the latter is due to trapped ions (see figure 17). However, the maximum power load in these 'hot spots' is of the order ~ 63 kW m^{-2}, below the tolerance of plasma-facing components of the machine. Preliminary studies of linear stability of Alfvénic modes driven by a population of EPs have been carried out as well for the Full Power scenario; a Maxwellian distribution function has been assumed, with constant EPs temperature (450 KeV) and an ITER like EP density profile. The study uses the HYMAGYC code, which is [56, 57] a recently developed HYbrid MAgnetohydrodynamics GYrokinetic Code suitable to study EP driven Alfvénic modes in general high-β axisymmetric equilibria, with perturbed electromagnetic fields fully accounted for. The thermal plasma is described by linear full resistive MHD equations in arbitrary axisymmetric equilibria. The coupling between MHD and EPs is obtained by adding to the MHD momentum equation a term proportional to $\nabla \cdot \Pi_k$ (Π_k being the EP stress tensor). Several EPs driven modes have been found using HYMAGYC. In figure 18 the growth-rate and frequency (normalized to the on-axis Alfvén frequency ω_{A0}) vs. the toroidal mode number n are shown: results for purely ideal MHD modes are shown using light blue open circles, infernal like modes driven by EPs are shown using black full circles, and EPs driven Alfvénic modes are shown using red diamonds. In figure 19, an example of the power spectra for a simulation considering the toroidal mode number $n = 10$ is shown: the first frame (left) is dominated by an EP driven mode (EPM) (early simulation phase, $t\omega_{A0} = 72$), the second frame (right) shows the appearance of a stronger infernal-like mode driven by EPs, with a frequency smaller (in absolute value) than the EPM (which is still observable). The Shear Alfvén and magneto/acoustic continua, as calculated by FALCON [58, 59] code are superimposed: larger and darker symbols refer to Alfvénic oscillations, while smaller and lighter ones to ion sound waves. Preliminary studies carried out with HMGC code [60] on model DTT equilibria, have demonstrated that the AE fluctuation spectrum in DTT is dominated by high toroidal mode number, $n \sim O(10–20)$, similar to ITER, characterized by an inner core region, dominated by reversed shear AEs (RSAEs), and an outer core region, dominated by toroidal AEs (TAEs) [61]. Meanwhile, different wave-EP resonances may be prevalent in the respective regions, and the global EP losses are ultimately determined by the interplay of transport processes due to the different fluctuations, with non-local non-linear dynamics playing a crucial role [62]. As anticipated in section 2, these non-linear dynamics reflect the unique role of EP as mediators of spatiotemporal cross-scale couplings in fusion plasma self-organization [10, 11]. It is worthwhile recalling that EP avalanches play a particularly important role in this respect and correspond to secular dynamics of long-lived structures in the EP phase space [63], which are undamped by fast collisionless processes and provide a description of an actual nonlinear plasma equilibrium in the presence of a finite fluctuation spectrum [64]. This suggests that weakly collisional reactor relevant fusion plasma be described as time evolving zonal states (ZS) [65], which consist of long-lived phase space zonal structures (PSZS),
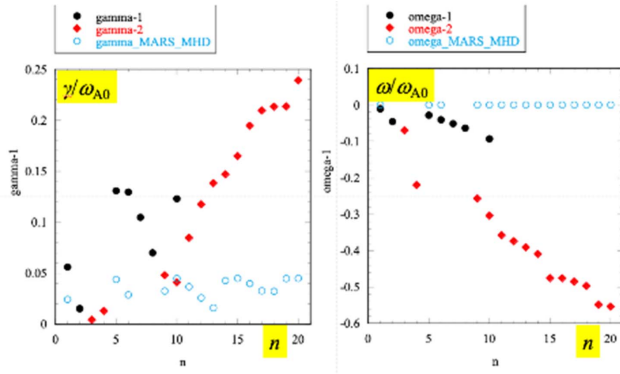
Figure 18. MARS and HYMAGYC results for a model full power DTT SN equilibrium.

together with the corresponding self-consistent zonal (toroidally symmetric) electromagnetic fields. Correspondingly, a novel approach to transport will be necessary for a proper description of these processes, which selectively occur in phase space not only for the EP component but for the core plasma as well [11, 66]. With its peculiar features, DTT will be a proper test bed for verification and validation of these novel approaches to the description of transport in reactor relevant fusion plasmas. Similarly, DTT will also be a proper test bed for verification and validation of fully global, electromagnetic, gyrokinetic numerical simulations, which are indispensable for the accurate prediction of the ZS evolution and of the corresponding nonlinear fluctuation spectra, as recently noted in [67].

## 6. Transient and off-normal events: a wind tunnel for ITER

Applying 3D resonant magnetic perturbations (RMPs) with non-axisymmetric saddle coils is a promising method to mitigate or suppress type-I Edge Localized Modes. DTT will be equipped with advanced systems to mitigate transient and off-normal events such as ELMs and disruptions respectively, with features similar to analogous systems present in ITER. In particular, within the DTT VV a system of 27 non-axisymmetric coils will be installed (NAS—i.e. three toroidal arrays of nine coils each) (figure 20), each independently powered and assembled in three toroidal rows with 9 coils each. For the purpose of ELM control, slowly rotating perturbations with toroidal mode number up to $n = 4$ can be applied. Preparatory modeling is ongoing and has been used so far to aid the design and predict coil current requirements. In particular linear plasma response modeling has been exploited to assess the effect of different coil geometries on ELM stability in full power operational scenarios. The MARS-F [68, 69] code has been used to compute, in toroidal geometry and including flow, the resistive plasma response to different vacuum fields with toroidal mode number $n = 1,2,3$. Preliminarily, two metrics have been used to link plasma response to ELM control. Namely the local normal plasma displacement in the

X-point region and the Chirikov parameter. An example of the magnetic field perturbations, optimized according to the X-point displacement criterion, is reported in figure 21. These criteria are used to predict optimal phasing of the active coil arrays and current thresholds based on empirical knowledge [70]. Depending on the number of active coils and on the scenario, coil currents between 20–30 kAt are predicted to be effective for ELM mitigation in DTT, with enough flexibility to accommodate other possible tasks that this sub-system should tackle during experiments. For example, the correction of Error Fields, or the possibility of using magnetic perturbations to interact with the rotation of (Neoclassical) TMs are foreseen as two major use-case for which dedicated studies are being carried out [71].

As for off- normal events, DTT will be equipped with a Disruption Mitigation System (DMS) based on the shattered pellet technique. Moreover, the complete DTT mechanical structures (FW, VV, magnets support, …) have been designed to sustain up to around 1000 disruption at the highest performances ($I_P = 5.5$ MA and 45 MW of injected power). Consequently, DTT is very well equipped to perform dedicated experimental campaigns to optimize the disruption control in ITER, a topic of outmost importance for its nuclear operation, as well as for the safe operation of any future fusion reactor based on the Tokamak concept. The estimate of the number of disruptions in DTT has been based on the [72, 73] experience gathered in similar class machines (JET, AUG, DIII-D and so on). Considering a 30% global disruptivity (including minor and mitigated disruptions), the maximum number of unmitigated events at full power has been estimated as 20% of the total number of disruptions. The structural assessment of the magnets, vessel and in-vessel components has been conservatively performed considering this number of disruptions and assuming that half of them could be vertical displacement events in the worst conditions.

The current and thermal quench characteristic times have been scaled as defined in [74] ITER Physics Basis and then the minimum linear CQ duration for DTT has been assumed equal to 4 ms. Slower disruption events have been also conservatively considered in the structural assessment of DTT, as highlighted by operations on [75] machines with metallic wall, to take care of the large EM and thermal loads that could be produced by larger and longer lasting halo currents typical of these events, in case of inefficient mitigation: the CQ duration for these events has been assumed equal to ten times the fastest ones, i.e. 40 ms.

The reference EM loads for the structural assessment have been calculated by performing a full set of simulations in different conditions (including Major Disruptions and VDE) with the 2D axisymmetric MAXFEA code and the 3D CARMA0NL code. The forces and paths of induced currents in 3D structures have been calculated also with ANSYS FEM code, using as input the plasma evolution calculated by MAXFEA. A further benchmark of the plasma evolution calculated by these codes will be carried out with simulations by MHD non-linear code JOREK. The DMS proposed for DTT consists in two (optionally four) multi-barrel Shattered Pellet
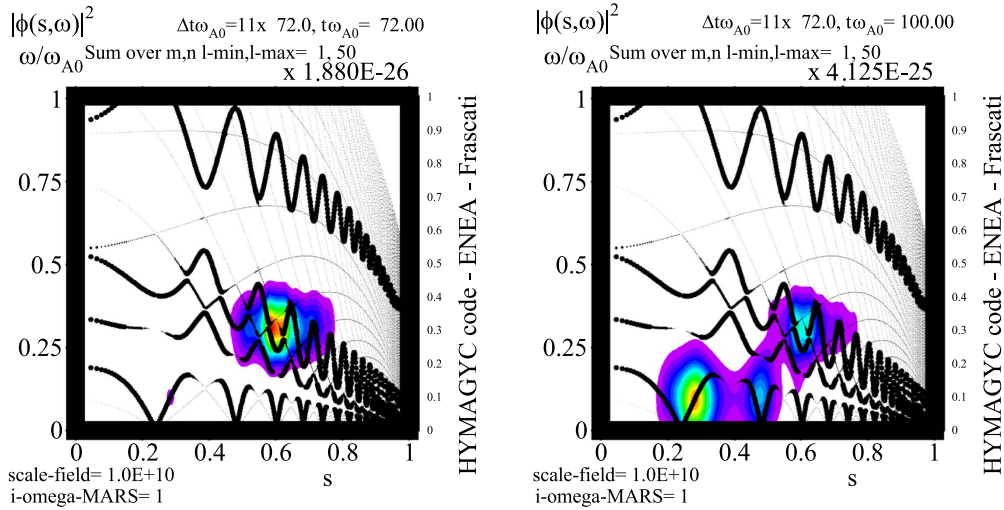
Figure 19. Frequency spectra of the electrostatic potential in the plane (s,ω) (here, s is the normalized radial coordinate and ω the frequency) as obtained by a linear HYMAGYC simulation considering the toroidal mode number $n = 10$: the colored structures refer to an energetic particle driven mode (left, $t\omega_{A0} = 72$) and to the appearance of the infernal-like mode (right, $t\omega_{A0} = 100$). Dots refer to Shear Alfvén and magneto/acoustic continua, as calculated by FALCON code; larger and darker symbols refer to Alfvénic oscillations, while smaller and lighter ones to ion sound waves.
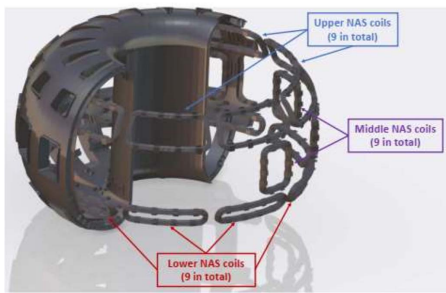
Figure 20. Three set of 9 NAS in three different poloidal locations.
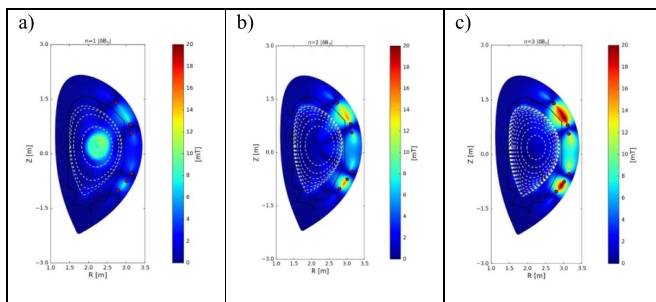
Figure 21. Normal perturbed magnetic field including plasma response for (*a*) $n = 1$ $Ic = 10$ kAt, (*b*) $n = 2$ $Ic = 20$ kAt, (*c*) $n = 3$ $Ic = 30$ kAt static perturbations. The black solid line represents roughly the inner DTT wall, white dashed contours mark rational surfaced for $n = 1,2,3$ and red dots indicate the positions on the poloidal plane of NAS coil legs (note that these coordinates are then adapted the local vacuum mesh when implemented in the code.

Injectors (SPI), capable to inject the number of particles necessary to trigger the thermal quench in plasmas of various currents and densities. The option of an additional Massive Gas Injection system has been considered to operate before the commissioning of the SPI. The SPIs will be located in two toroidally opposite upper oblique ports. Given a maximum total thermal energy in DTT plasmas around 14 MJ (including fast ions), the pellet dimension can be preliminary estimated as 10^{23} atoms (corresponding about to a 14 mm pellet), injected with a velocity greater than 300 ms, in order to guarantee a flight time well below 10 ms. The JOREK simulations will assess also whether this two SPIs solution is appropriate for mitigation or if other two SPIs (in vertical or horizontal ports) are required.

7. DTT research plan (DTT-RP)

The DTT-RP, is currently in writing by a large group of about 100 European Scientists, from most EU countries involved in fusion research. The DTT-RP is intended to be a living document that will have to evolve along the DTT construction phase, following all the international experimental and theoretical progresses, to prepare at the best the exploitation of the machine.

A first draft of the Research Plan has already been produced, and it has provided the DTT documentation for the ongoing EUROfusion facility review. The work is the result of six different expert groups: EG1, DTT scientific exploitation strategy; EG2, Divertor and SOL physics; EG3, Plasma scenarios and associated modeling; EG4, Heating, current drive and fuelling; EG5, MHD and EPs, theory; EG6, Fusion technology developments. The RP will consist of 9 different Chapters (Chapter 1: DTT power exhaust strategy; Chapter 2: Plasma scenarios; Chapter 3: Divertor and SOL physics; Chapter 4: Transport physics & integrated modeling; Chapter 5: MHD, disruptions and control; Chapter 6: Physics of heating, current drive and fuelling; Chapter 7: Energetic particle physics; Chapter 8: Theory and simulation; Chapter 9: Fusion technology developments). Moreover, a set of Appendices will
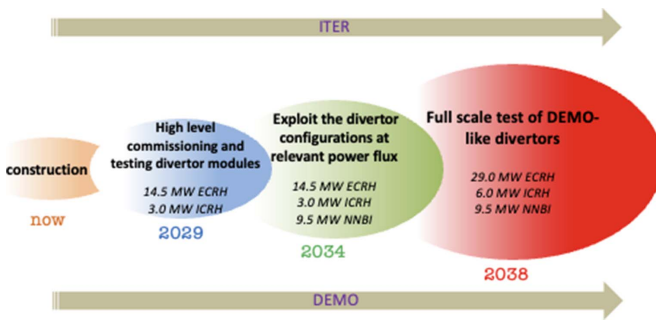
Figure 22. The three main phases of the DDT planned experimental life. All the quoted additional power are intended as coupled power.

shortly describe the main technical features. The RP is being written along the following general guidelines:

(a) DTT has a set of unique characteristics: high field, high current, high density and low collisionality, full W, long pulse, EP population with typical pressures comparable with the thermal component and characteristic energy higher than critical, dominant electron heating and low torque.

(b) DTT main missions are: validation of optimum power exhaust strategy for DEMO and related plasma scenarios, with full core-edge integration at high performance; support to the various phases of ITER exploitation.

(c) DTT exploitation life will have essentially three main phases (figure 22—targeting as first plasma the end of 2029), that will go in parallel to ITER experimental program and with the final choices about the DEMO construction.

These three phases are:

(1) High level commissioning phase at reduced plasma current ($I_p \sim 2 \div 3$ MA) and, initially at half toroidal field (for coupling the ECRH at the second harmonic); during this phase the additional heating will be increased from the 8 MW of ECRH, foreseen to be available for the first plasma, up to 14.5 MW of ECRH plus 3 MW of ICRH. Along this period, all the main equilibrium configurations will be tested and the plasma discharge will be extended up to 50 s, with a significant power flux on the divertor tiles (up to 5 MW m^{-2}), which will include actively cooled W PFCs operations. At these reduced performances, DTT will be also able to explore advanced regimes at high β_N and, consequently, to be complementary to the JT-60SA research program.

(2) Along the DTT second phase, additional 9.5 MW of NNBI will be included, increasing the possible total flux flowing to the divertor tiles up to around 10 MW m^{-2}. The DTT divertor will be equipped with 'test modules' divertor sectors, located in four different toroidal location, just in front of a dedicated port which will allow an 'easy' replacement of the test modules; these divertor test modules will allow testing and comparing different materials and partially the local shaping of the divertor PFUs. Note that all along

these two phases DTT will operate in parallel to ITER, consequently a strong connection with the ITER RP will have to be considered.

(3) Eventually, along the third phase DTT will operate at the highest performances, a new divertor will be possibly installed and experimentally studied, in order to propose a viable and experimentally validated solution for the DEMO divertor. Finally, the first issue of the DTT-RP will work out an ideal experimental program considering these three phases, but it will also deal with the input necessary to finalize the DTT construction (for instance on the required plasma diagnostics).

8. Conclusions

DTT is intended to be an experimental facility, open to international collaborations, supporting the exploitation of ITER and of other experiments and along the DEMO design finalization phase. Its unique properties (high toroidal field, high density, low collisionality and a possible divertor power flow even larger than the present materials capabilities) make DTT an important (and maybe unique) experiment finalized to tackle the most important integrated technical and physical aspects to be solved before the realization of a fusion power plant. Having the same dimensionless most important physics parameters close to the ITER ones, the same full tungsten plasma facing material (both for the FW and the divertor), a similar additional heating scheme, makes DTT the perfect experiment to support at best the ITER experiments to achieve its final targets. Moreover, having a unique possibility to test different divertor ideas (materials as well as divertor shapes), including the possibility to quickly test new ideas by using the TMDs, at power fluxes divertor relevant ($P/R \sim 15$ MW m^{-1}), makes DTT the optimal experiment to find a solution to challenging power exhaust problem as an integrated core-edge problem.

Acknowledgments

ORCID iDs

M.V. Falessi ● https://orcid.org/0000-0002-2105-226X

P. Mantica [icon] https://orcid.org/0000-0001-5939-5244

G. Vlad [icon] https://orcid.org/0000-0003-1482-5436

R. Albanese [icon] https://orcid.org/0000-0003-4586-8068

E. Alessi [icon] https://orcid.org/0000-0002-8750-9867

C. Angioni [icon] https://orcid.org/0000-0003-0270-9630

P. Agostinetti [icon] https://orcid.org/0000-0003-2103-7630

B. Baiocchi [icon] https://orcid.org/0000-0002-1483-3113

L. Balbinot [icon] https://orcid.org/0000-0002-7467-533X

T. Bolzonella [icon] https://orcid.org/0000-0003-1128-964X

S. Brezinsek [icon] https://orcid.org/0000-0002-7213-3326

References

[1] DTT 2019 DTT interim design report (available at: www.dtt-project.enea.it/downloads/DTT_IDR_2019_WEB.pdf)

[2] Romanelli M. *et al* 2014 JINTRAC: a system of codes for integrated simulations of tokamak scenarios *Plasma Fusion Res.* **9** 3403023

[3] Pereverzef G. and Yushmanov P.N. 1991 ASTRA Automated System of Transport in a Tokamak *Max Plank Institute für Plasmaphysik* IPP 5/42

[4] Fable E. *et al* 2013 *Nucl. Fusion* **53** 033002

[5] Staebler G.M. *et al* 2022 *Nucl. Fusion* **62**

[6] Bourdelle C. *et al* 2016 *Plasma Phys. Control. Fusion* **58** 076028

[7] Romanelli F. *et al* 2024 Divertor Tokamak Test facility Project: status of design and implementation *Nucl. Fusion* **64** 112015

[8] Pizzuto A. *et al* 2023 The divertor tokamak test facility: engineering and technology integration challenges—TECH/2-2 *29th IAEA Fusion Energy Conf. (FEC 2023)* (*London, October 2023*)

[9] Stix T.H. 1972 *Plasma Phys.* **14** 367

[10] Zonca F., Chen L., Briguglio S., Fogaccia G., Milovanov A.V., Qiu Z., Vlad G. and Wang X. 2015 Energetic particles and multi-scale dynamics in fusion plasmas *Plasma Phys. Control. Fusion* **57** 014024

[11] Chen L. and Zonca F. 2016 Physics of Alfvén waves and energetic particles in burning plasmas *Rev. Mod. Phys.* **88** 015008

[12] and E.D.I.T.O.R.S. *et al* 2007 *Nucl. Fusion* **47** s1–s17

[13] Federici G. *et al* 2019 *Nucl. Fusion* **59** 066013

[14] Siccinio M. *et al* 2020 *Fusion Eng. Des.* **156** 111603

[15] Barabaschi P. *et al* 2023 Progress on ITER manufacturing, construction, commissioning and plans—OV/1-3 *29th IAEA Fusion Energy Conf. (FEC 2023)* (*London*)

[16] Kadomtsev B.B. 1975 *Sov. J. Plasma Phys.* **1** 295

[17] Lackner K., Coster D. and Schneider R. (The ASDEX-Upgrade Team) 1998 *Czech. J. Phys.* **48** 167

[18] Crisanti F. *et al* 2017 The DTT device: rationale for the choice of the parameters *Fus. Eng. Design* **122** 288–98

[19] Pizzuto A. *et al* 2010 *Nucl. Fusion* **50** 095005

[20] Casiraghi I. *et al* 2023 *Plasma Phys. Control. Fusion* **65** 035017

[21] Bonanomi N. *et al* 2023 Full-radius time-dependent simulations of the DTT tokamak plasmas *49th EPS Conf. on Plasma Physics—Mo_MCF37* (*Bordeaux*)

[22] Saarelma S. *et al* 2018 *Plasma Phys. Control. Fusion* **60** 099601

[23] Fajardo D. *et al* 2022 *Plasma Phys. Control. Fusion* **64** 055017

[24] Baiocchi B., Aucone L., Casiraghi I., Figini L., Koechl F. and Mantica P. 2023 *Nucl. Fusion* **63** 106009

[25] Mariani A. *et al* 2024 First-principle based predictions of the effects of negative triangularity on DTT scenarios *Nucl. Fusion* **64** 046018

[26] Balestri A. *et al* 2024 *Plasma Phys. Control. Fusion* **66** 075012

[27] Aucone L. *et al* 2024 *Plasma Phys. Control. Fusion* **66** 075013

[28] Mariani A. *et al* Negative triangularity scenarios: from TCV and AUG experiments to DTT predictions *This Conf*.

[29] Bufferand H. *et al* 2013 Near wall plasma simulation using penalization technique *J. Nucl. Mater.* **438** S445–S448,438

[30] Bufferand H. *et al* 2015 Numerical modelling for divertor design of the WEST *Nucl. Fusion* **55** 053025

[31] Eich T. *et al* 2011 *Phys. Rev. Lett.* **107** 215001

[32] Eich T. *et al* 2013 Scaling of the tokamak near the scrape-off layer H-mode *Nucl. Fusion* **53** 093031

[33] Balbinot L., Rubino G., Casiraghi I., Meineri C., Frassinetti L., Aucone L., Mantica P., Innocente P. and Wigram M. 2023 *Nucl. Mater. Energy* **34** 101350

[34] Innocente P. *et al* 2022 *Nucl. Mat. and Energy* **33** 101276

[35] Innocente P., Ambrosino R., Brezinsek S., Calabrò G., Castaldo A., Crisanti F., Dose G., Neu R. and Roccella S. 2022 *Nucl. Mater. Energy* **33** 101276

[36] Pitts R.A. *et al* 2019 *Nucl. Mater. Energy* **20** 100696

[37] Tantos C. *et al* 2024 *Nucl. Fusion* **64** 016019

[38] Fusco V. *et al* 2022 *47th EPS Conf. on Plasma Physics. European Physical Society* (*Virtual*) (available at: http://ocs.ciemat.es/EPS2022PAP/pdf/P2a.125.pdf)

[39] Lutjens H., Bondeson A. and Sauter O. 1996 *Comp. Phys. Comm.* **97** 219–60

[40] Bondeson A., Vlad G. and Lutjens H. 1992 *Phys. Fluids* **B4** 1889–900

[41] Fasoli A. 2016 Computational challenges in magnetic-confinement fusion physics *Nat. Phys.* **12** 411–23

[42] Pigatto L. *et al* 2024 Numerical investigation of toroidal plasma response for ELM control via magnetic perturbations in the DTT Tokamak *Nucl. Fusion* **64** 016023

[43] Sauter O. *et al* 2002 *Phys. Rev. Lett.* **88** 105001

[44] Basiuk V., Huynh P., Merle A., Nowak S. and Sauter O. 2017 *Plasma Phys. Control. Fusion* **59** 125012

[45] Kalupin D. *et al* 2013 *Nucl. Fusion* **53** 123007

[46] Cenacchi G. and Taroni A. 1988 A free boundary plasma transport code (basic version) ENEA RT/TIB/88/5 ENEA—Report JET-IR (88) 0

[47] White R.B. and Chance M.S. 1984 *Phys. Fluids* **27** 2455

[48] Hirvijoki E., Asunta O., Koskela T., Kurki-Suonio T., Miettunen J., Sipilä S., Snicker A. and Äkäslompolo S. 2014 *Comput. Phys. Commun.* **185** 1310–20

[49] Spizzo G. *et al* 2021 *Nucl. Fusion* **61** 116016

[50] Vincenzi P. *et al* 2023 *Fusion Eng. Des.* **189** 113436

[51] Li Y., Falessi M.V., Lauber P., Li Y., Qiu Z., Wei G. and Zonca F. 2023 Physics of drift Alfvén instabilities and energetic particles in fusion plasmas *Plasma Phys. Control. Fusion*

[52] Vlad G. *et al* 2021 *Nucl. Fusion* **61** 116026

[53] Asunta O., Govenius J., Budny R., Gorelenkova M., Tardini G., Kurki-Suonio T., Salmi A. and Sipilä S. 2015 *Comput. Phys. Commun.* **188** 33–46

[54] de Piccoli E.A. *et al* 2023 Evaluation of DTT NBI energetic particle confinement and prompt-losses through the constant of motion phase space *49th EPS Conf. on Plasma Physics* (*Bordeaux*)

[55] Gobbin M. and Spizzo G. 2023 ORBIT simulations of fast ion power loads on the wall of the Divertor Tokamak Test *Plasma Phys. Control. Fusion* **65** 075013

[56] Vlad G. *et al* *11th IAEA Technical Meeting on Energetic Particles in Magnetic Confinement Systems* (*Kyiv, 21–23 September 2009*) (International Atomic Energy Agency) (available at: https://www.qst.go.jp/site/jt60-english/6043.html)

[57] Fogaccia G., Vlad G. and Briguglio S. 2016 *Nucl. Fusion* **56** 112004

[58] Falessi M.V., Carlevaro N., Fusco V., Giovannozzi E., Lauber P., Vlad G. and Zonca F. 2020 *J. Plasma Phys.* **86** 845860501

[59] Falessi M.V., Carlevaro N., Fusco V., Vlad G. and Zonca F. 2019 *Phys. Plasmas* **26** 082502

[60] Briguglio S., Vlad G., Zonca F. and Kar C. 1995 Hybrid magnetohydrodynamic-gyrokinetic simulation of toroidal Alfvén modes *Phys. Plasmas* **2** 3711

[61] Wang T. *et al* 2018 Shear Alfvén fluctuation spectrum in divertor tokamak test facility plasmas *Phys. Plasmas* **25** 062609

[62] Wang T., Wang X., Briguglio S., Qiu Z., Vlad G. and Zonca F. 2019 Nonlinear dynamics of shear Alfvén fluctuations in divertor tokamak test facility plasmas *Phys. Plasmas* **26** 012504

[63] Zonca F., Chen L., Briguglio S., Fogaccia G., Vlad G. and Wang X. 2015 *New J. Phys.* **17** 013052

[64] Falessi M.V. and Zonca F. 2019 *Phys. Plasmas* **26** 022305

[65] Falessi M.V., Chen L., Qiu Z. and Zonca F. 2023 *New J. Phys.* **25** 123035

[66] Lauber P. *et al* 2024 ATEP: an advanced transport model for energetic particles *Nucl. Fusion* **64** 096010

[67] Chen L., Qiu Z. and Zonca F. 2023 *Nucl. Fusion* **63** 106016

[68] LIU Y.Q., BONDESON A., Fransson C.-M., Lennartson B. and Breitholtz C. 2000 *Phys. Plasmas* **7** 3681–90

[69] Liu Y.Q., Kirk A. and Nardon E. 2010 *Phys. Plasmas* **17** 122502

[70] Pigatto L., Bolzonella T. Bonotto M, Fusco V, Liu YQ, Marchiori G, Villone F and Vlad G 2023 *Nucl. Fusion* **61** 016023

[71] Albanese R. and Bolzonella T. 2023 *Fusion Eng. Des.* **189** 113437

[72] Gerhardt S.P. *et al* 2013 *Nucl. Fusion* **53** 04302

[73] de Vries P.C., Johnson M.F., Alper B., Buratti P., Hender T.C., Koslowski H.R. and Riccardo V. 2011 *Nucl. Fusion* **51** 053018

[74] Hender T.C. *et al* 2007 Progress in the ITER physics basis chapter 3: MHD stability, operational limits and disruptions 2007 *Nucl. Fusion* **47** S128–202

[75] Lehnen M. *et al* 2013 *Nucl. Fusion* **53** 093007